J. Fluid Mech. (2013), *vol.* 730, *pp.* 245–272.
doi:10.1017/jfm.2013.341

Ultrasonic cavitation near a tissue layer

G. A. Curtiss[1], D. M. Leppinen[2,†], Q. X. Wang[2] and J. R. Blake[2]

[1]Numerical Algorithms Group, Oxford OX2 8DR, UK

[2]School of Mathematics, University of Birmingham, Edgbaston, Birmingham B15 2TT, UK

(Received 3 April 2013; revised 3 April 2013; accepted 25 June 2013;
first published online 30 July 2013)

In this paper we examine the dynamics of an initially stable bubble due to ultrasonic forcing by an acoustic wave. A tissue layer is modelled as a density interface acted upon by surface tension to mimic membrane effects. The effect of a rigid backing to the thin tissue layer is investigated. We are interested in ultrasound contrast agent type bubbles which have immediate biomedical applications such as the delivery of drugs and the instigation of sonoporation. We use the axisymmetric boundary integral technique detailed in Curtiss *et al.* (*J. Comput. Phys.*, 2013, submitted) to model the interaction between a single bubble and the tissue layer. We have identified a new peeling mechanism whereby the re-expansion of a toroidal bubble can peel away tissue from a rigid backing. We explore the problem over a large range of parameters including tissue layer depth, interfacial tension and ultrasonic forcing.

Key words: bubble dynamics, cavitation, drops and bubbles

1. Introduction

Industrial and military uses for cavitation have now long been established. Recent advances in medicine, however, have created new avenues for cavitation, thus motivating the current research. The phenomenon, originally occurring as an unwanted side effect, is now being developed as an effective, targetable mechanism for damaging organic structures. It is particularly prevalent in various types of laser surgery. These include techniques such as laser angioplasty, myocardial laser revascularization, laser thrombolysis and intraocular photodisruption (Brujan *et al.* 2001*a*). Figure 1 shows an experimental example of the type of damage which may be inflicted upon a cornea during intraocular photodisruption. Here a bubble has been created using a focused laser beam parallel to a cornea specimen at a standoff distance of 0.45. The result of the subsequent collapse of this cavity is very apparent, with a puncture clearly visible in the centre of the affected region almost certainly created by the high-speed jet that would have threaded the bubble. A large region of surface tissue has also been scrapped away during the bubble motions. The mechanisms for this are as yet unknown, with the high shear stresses caused by the high-speed flow between the bubble and substrate thought to be a contributing factor (Vogel *et al.* 1990; Brujan *et al.* 2001*a*). In this paper we demonstrate that the re-expansion of the bubble toroid plays a significant role, and may indeed be the primary mechanism for such surface scouring.

† Email address for correspondence: D.M.Leppinen@bham.ac.uk

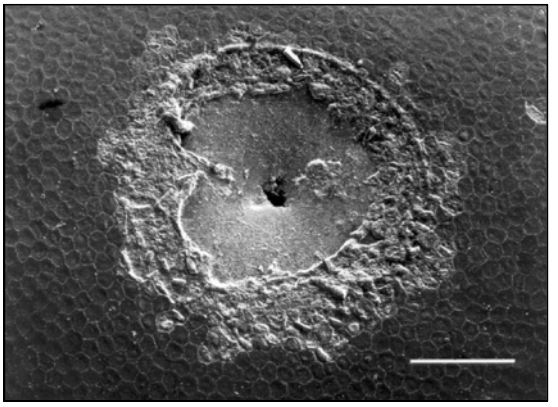

FIGURE 1. Cavitation damage to a cornea specimen. The white scale bar represents a distance of 100 μm, whilst the laser generated bubble was formed at a standoff distance of 0.45 maximum bubble radii (Vogel *et al.* 1990).

Aside from laser-generated high-pressure bubbles, sonically driven cavitation is also prevalent in modern medical procedures. One such procedure is shockwave lithotripsy, where a semi-ellipsoidal structure is placed adjacent to a patient, focusing shockwaves generated at the external focus to the focus located inside the body. Removal of kidney and bladder stones via this procedure benefits from the collapse phenomena, with the focusing of the shockwave creating tiny cavities close to the surface of the target object. The side effects of this technique, potentially magnified by unwanted cavitation, can be problematic and can include major vein thrombosis and gastrointestinal injuries such as colon perforation (Skolarikos, Alivizatos & Rosette 2006).

Other medical techniques have been developed using both low- and high-frequency ultrasound to acoustically activate cavitation during diagnostic procedures. The use of ultrasound contrast agents (UCAs) to improve the echogenicity of biological fluids is one such technique. These are encapsulated micrometre-scale gas bubbles with thin shells, which can be easily administered to a patient through injection or ingestion. Examples of such products include protein shelled encapsulated air UCAs such as Albunex, and modern soft lipid-shelled perfluorocarbon-encapsulated UCAs such as SonoVue (Marmottant *et al.* 2005; Cosgrove 2006). The acoustic signature produced by the compressible UCAs is significantly higher than that of the near-incompressible tissues, and provides great improvement in visualization, particularly in detecting focal liver lesions (Church 1995; Blomley *et al.* 2001; Cosgrove 2006).

At higher ultrasound amplitudes, UCAs will break down in the acoustic field. This structural failure allows for their potential use as locally targetable drug delivery vesicles (Seemann *et al.* 2002; Rapoport *et al.* 2003; Cosgrove 2006). Of particular note is the manner in which breakdown occurs, and the damage it can cause to surrounding tissue. An example of the damaging effect caused by such operations can be seen in figure 2, showing samples of mouse abdominal muscle after ultrasound exposure, using a 2.5 MHz transducer at an amplitude of 2.6 MPa with and without the contrast agent Optison. Petechial haemorrhages are visible in abundance as dots and streaks in the agent-treated sample, yet there are few, if any, in the untreated case (Miller & Quddus 2000).

This seemingly unwanted side affect has recently been pioneered as a local delivery method for large molecules. In particular, it can be used to deliver DNA, and hence

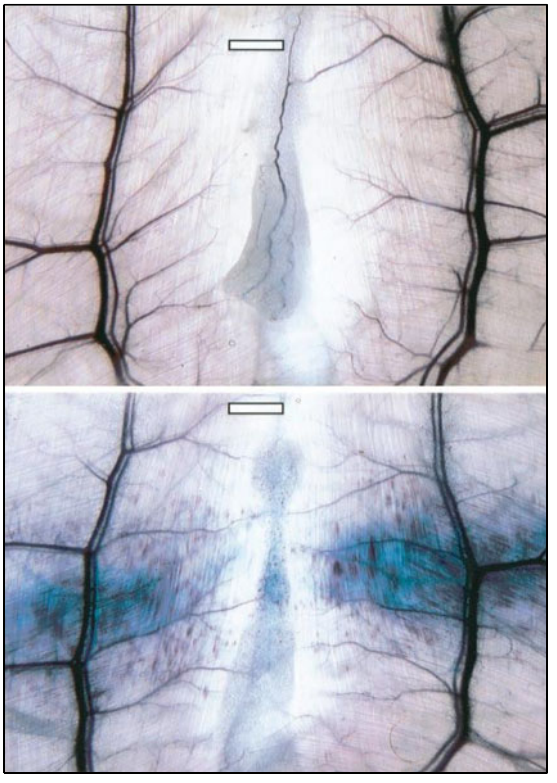

FIGURE 2. (Colour online) Abdominal mouse muscle and fat after ultrasound exposure using a 2.5 MHz transducer at an amplitude of 2.6 MPa. The contrast agent Optison was used in the specimen displayed in the lower image. Abundant petechial haemorrhages are visible in the lower sample as dots and streaks. The scale bar represents 1 mm (Miller & Quddus 2000).

is being actively researched as a non-viral method for gene transfection (Miller, Bao & Thrall 1997; Blomley *et al.* 2001; Miller, Pislaru & Greenleaf 2002). This process, termed sonoporation, involves the local induction of cavitation dynamics using ultrasound to permeate cell membranes, thereby allowing DNA introduced into the extracellular environment to enter the target cells (Miller *et al.* 1997). The potential benefits of sonoporation over existing transfection techniques are considerable. Viral encapsulation delivery systems suffer from possible toxicological and mutagenic side effects, whilst other encapsulation techniques such as lipid coating, are not locally focusable Miller *et al.* (2002). Locally targeted non-encapsulation methods also exist, although these have difficulties with implementation. Electroporation for example requires electrodes to be inserted into the target area to induce cell membrane separation, and the direct injection of DNA into cells is naturally restricted to external applications. Transfection through sonoporation in contrast is easily administered externally, and is readily locally focused. Excessive cavitation caused during the application can however cause significant damage and cell death (Koike *et al.* 2005), with the generation of sonopores with size on the order of the magnitude of a cell (Prentice *et al.* 2005). To minimize the amount of cell death, and to determine the mechanisms from which it arises, the fluid dynamics of both the intracellular and extracellular environments need to be examined. Similarly to help maximize the viable

poration of cell membranes, the dynamics associated with the collapse of the UCAs is of critical importance.

The organic environments with which these cavities interact cannot, in general, be viewed simply as rigid boundaries. Aside from the complex topology of the surroundings, the elasticity of the cell membranes and the fluid which they enclose must be taken into consideration. This is evident from recent experiments with initially flat elastic surfaces. These have shown that the elastic modulus of the substrate and the standoff distance of the interacting bubble have drastic effects on the bubble dynamics, both with regards to the translation of the bubble and the jet direction (Brujan *et al.* 2001*a*,*b*). Indeed in some cases horizontal bubble splitting is observed, resulting in very slender high-speed jets forming in opposing directions. This potentially has a significant impact on membrane permeation, and explains the significant maximum bubble radius to jet width ratio of 60:1 observed in the experiment shown in figure 1.

Recent numerical investigations using the boundary integral method by Klaseboer & Khoo (2004*a*,*b*) accounting for these interfacial properties have shown qualitative agreement with such experiments. In their simulations, it was assumed that the jump in tangential velocities across the fluid–fluid interface was sufficiently small to be neglected from the dynamic boundary conditions, with marginal discrepancies observed in their test cases. The procedure employed depended upon a geometrical argument valid for a single bubble in an infinite fluid, utilizing the trivial density ratio of 1. This allowed for the interfacial potential in the cavitated fluid to be found independently of the normal velocity of the two-fluid interface, by equating various aspects of the coefficient matrices. Elastic effects were also investigated by means of a modification to the pressure in the fluid not containing the cavitation, and hence a modification to the dynamic condition on the liquid–liquid boundary (Klaseboer & Khoo 2004*b*). This showed marked differences to the case where no elasticity is present, allowing for the aforementioned bubble splitting to be observed. Further investigations using this implementation have researched acoustically driven bubble behaviour at subatmospheric pressure amplitudes near an interface given realistic biological parameters, demonstrating some of the shapes the bubbles may attain during pre-toroidal motions (Fong *et al.* 2006). As in the experiments near-elastic interfaces, these simulations have shown bubble motion and jet direction to both be affected by the properties of the material. Prior to the research contained herein, however, toroidal effects have not been investigated in this context.

Coupled boundary-integral/finite-element numerical implementations have recently been developed to account for elastic boundaries near bubbles. Miao & Gracewski (2008) used this to simulate linearly elastic axisymmetric interactions, both of a bubble near an infinite elastic surface and a bubble confined in an elastic tube. The results for the infinite plate were in agreement with the experiments of Brujan *et al.* (2001*a*), and the tube encapsulated simulations have shown the generation of ellipsoidal bubbles and consequent perpendicular pinching behaviour. The limitation of the axisymmetric geometry however did not permit off-centre interactions, as the development of jets towards the tube walls was impossible. Three-dimensional interactions with a toroidal bubble and an elastic plate have also been simulated by Klaseboer *et al.* (2005) in the context of an underwater explosion, using a boundary integral/vortex ring method for the fluid dynamics coupled with a finite-element model for the plate. This was successful in capturing the plastic deformations to a steel plate caused by the dynamics associated with a collapsing explosion bubble.

This paper examines the non-spherical behaviour of ultrasound activated microbubbles, directly relevant to the new biomedical procedure sonoporation. The

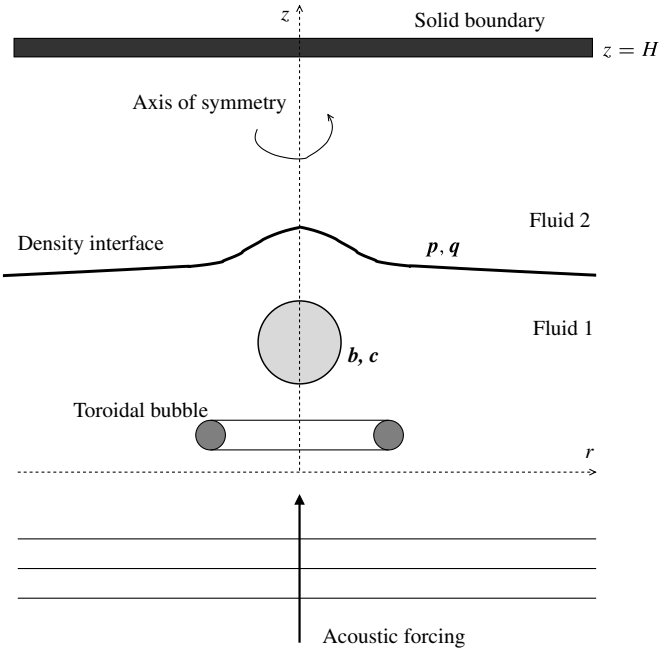

FIGURE 3. The axisymmetric geometry used to model the interaction of a bubble with a density interface near a solid boundary.

influence of a tension laden membrane boundary is investigated using practical density ratios, showing significant deviations in bubble shape from the spherical mode. Moreover, the influence of a solid backing to a cell layer is investigated, and has demonstrated new phenomena. These include the peeling of the cell layer by the re-expanding toroidal bubble when the cell layer depth is sufficiently less than the maximum bubble radius, as well as the injection behaviour generated by smaller bubbles under high driving frequencies near thicker layers. It is clearly demonstrated that the jet may cause significant damage to the cell layer, implying that the targeting of cells for transfection using ultrasound activated contrast agents should include the expected non-spherical behaviour after jet impact has occurred.

2. Mathematical model

In this paper we are interested in the dynamics of bubbles near a tissue layer due to ultrasonic forcing. Thus, we have to slightly modify the mathematical model presented in Curtiss *et al.* (2013) which considered the dynamics of bubbles with a constant pressure in the far field. Briefly, the problem we are considering is sketched in figure 3 with a layer of fluid of density ρ_1 underlying a layer of fluid of density ρ_2 with $\rho_2 \leqslant \rho_1$. We assume axisymmetric cylindrical coordinates (r, z) as indicated. Initially the density interface is flat and is located at $z = 0$. In the rigid backing simulations we place a solid boundary at $z = H$ so that fluid 2 is of finite depth. Alternatively, we can choose to put a solid boundary at $z = -H$ so that fluid 1 is of finite depth. In either case we will only consider situations where there is one bubble which is located in the fluid of infinite depth. The formulation below is for the case when fluid 2 is of finite depth.

As in Curtiss *et al.* (2013) we assume that in each layer the fluid is inviscid, incompressible and irrotational. Thus, the velocity field in each fluid layer can be written as the gradient of a potential with

$$\boldsymbol{u}_i = \nabla \phi_i \tag{2.1}$$

for $i = 1, 2$ where

$$\nabla \cdot \boldsymbol{u}_i = \nabla^2 \phi_i = 0 \tag{2.2}$$

and

$$\nabla \times \boldsymbol{u}_i = \boldsymbol{0}. \tag{2.3}$$

We consider the case of a single bubble located in the lower layer. The bubble is initially spherical and its centroid is a distance z_c below the density interface. For the micrometre-sized bubbles which are of interest for biomedical applications gravitational effects can be ignored. Thus in each fluid layer we can write Bernoulli's equation to give

$$\frac{\partial \phi_i}{\partial t} + \frac{|\boldsymbol{u}_i|^2}{2} + \frac{p}{\rho_i} = \frac{p_\infty}{\rho_i} \tag{2.4}$$

where t is time, p is pressure and p_∞ is the far-field pressure. The acoustic wave is modelled through a time-dependent pressure term from the far field with

$$p_\infty(z, t) = \bar{p}_\infty + \tilde{p}_\infty \sin(kz - \omega t) \tag{2.5}$$

where $\bar{p}_\infty$ is the background pressure at infinity, $\tilde{p}_\infty$ is the amplitude of the acoustic forcing, and $k = 2\pi f c^{-1}$ and $\omega = 2\pi f$ are the wavenumber and radial frequency given the speed of sound of the liquid c and the frequency of the wave f.

We note here that a travelling pressure wave will cause fluid motion in the z direction. The behaviour of any cavitation bubbles will also be affected by their location with respect to the pressure peaks and troughs. In this work however the magnitude of this motion is assumed to be negligible in comparison to the motion induced by the expanding cavity. Hence, in all cases here, a standing wave is used as opposed to a travelling wave. Whilst this is certainly expected to be valid near a rigid boundary due to wave reflection, it is not necessarily realistic in free field environments. It makes little difference however as the typical wavelength is at least an order of magnitude greater than the length scale on which the bubbles oscillate. For example, a wave with frequency 0.2 MHz and peak pressure 1.4 MPa will have a wavelength of approximately 7000 μm in water, and will cause a spherical cavitation bubble initially at equilibrium with a radius of 2.5 μm to grow to approximately 75 μm. In addition, the focus of this work is on the inertial effects of the cavitation bubbles, which in the situations envisaged here will most likely dominate. More violent shockwave interactions are beyond the scope of this work, although various methods have been developed to incorporate them into boundary integral simulations (Calvisi, Iloreta & Szeri 2008).

Our analysis now follows directly from Curtiss *et al.* (2013) except that we note that the p_∞ term in our Bernoulli equations is given by (2.5). We proceed by non-dimensionalizing our equations as detailed in table 1: we use the density of the lower layer, ρ_1, for density; the difference in the far-field pressure and the condensible gas vapour pressure, $\Delta p = \bar{p}_\infty - p_v$, for pressure; the maximum radius a bubble would reach in an infinite fluid of density ρ_1, R_{max} for length; $R_{max}(\rho_1/\Delta p)^{1/2}$ for

$(\bar{r}, \theta, \bar{z}) = \left(\dfrac{r}{R_{max}}, \theta, \dfrac{z}{R_{max}}\right)$	The non-dimensional cylindrical coordinate system.
$\Delta_p = \bar{p}_\infty - p_v$	The dimensional pressure difference between the far-field and bubble vapour pressures.
$\bar{t} = \dfrac{t}{R_{max}}\sqrt{\dfrac{\Delta_p}{\rho_1}}$	The non-dimensional time scale.
$h = \lvert\bar{z}_c(\bar{t}=0)\rvert = \dfrac{\lvert z_c\rvert}{R_{max}}$	The dimensionless standoff distance h, corresponding to the ratio of the absolute value of the initial vertical bubble centroid $\bar{z}_c$ to R_{max}.
$\bar{\phi}_i = \phi_i R_{max}\sqrt{\dfrac{\rho_1}{\Delta_p}}$	The non-dimensional potential in layer i.
$\rho = \dfrac{\rho_2}{\rho_1}$	The ratio of liquid densities.
$\epsilon = \dfrac{p_0}{\Delta_p}$	The non-dimensional strength parameter.
$\tilde{\epsilon} = \dfrac{\tilde{p}_\infty}{\Delta_p}$	The non-dimensional amplitude of the acoustic forcing.
$\delta = \dfrac{\rho_1 g R_{max}}{\Delta_p}$	The buoyancy parameter.
$\bar{\sigma}_b = \dfrac{\sigma_b}{R_{max}\Delta_p}$	The surface tension along a bubble surface.
$\bar{\sigma}_I = \dfrac{\sigma_I}{R_{max}\Delta_p}$	The surface tension along the density interface.

TABLE 1. Dimensional and non-dimensional parameters and variables. The non-dimensional parameters are indicated by an overbar when ambiguity arises.

time; $(\Delta p/\rho_1)^{1/2}/R_{max}$ for potential; $R_{max}\Delta p$ for surface tension. The length scale R_{max} is the maximum radius a bubble initially in equilibrium would attain in an infinite ambient subject to the imposed acoustic wave. An important parameter in bubble dynamics is the standoff distance, h, which is the dimensionless ratio of the initial vertical displacement of a bubble centroid z_c from a boundary to R_{max} defined as $h = |z_c|/R_{max}$. Using these scales the dimensionless evolution equation for ϕ_1 along the surface of the bubble in fluid 1 is given by

$$\frac{\mathrm{D}\phi_1}{\mathrm{D}t} = \frac{|\boldsymbol{u}_1|^2}{2} + 1 - \epsilon\left(\frac{V}{V_0}\right)^\gamma + \sigma_b \nabla\cdot\boldsymbol{n}_b + \tilde{\epsilon}\sin(kz - \omega t). \tag{2.6}$$

Along the fluid–fluid interface we define

$$F = (\phi_1 + \phi_2)(1-\rho) + (\phi_1 - \phi_2)(1+\rho) \tag{2.7}$$

where $\rho = \rho_2/\rho_1$. The evolution equation for F satisfies

$$\frac{\mathrm{D}F}{\mathrm{D}t} = (1-\rho)\boldsymbol{u}_1\cdot\boldsymbol{u}_2 + 2\sigma_I\nabla\cdot\boldsymbol{n}. \tag{2.8}$$

At time $t = 0$ we assume that both fluid layers are motionless and that the bubble in layer 1 has an initial radius of R_0 and that it is in equilibrium with a constant far-field

pressure $\bar{p}_\infty$. This requires that

$$\epsilon = \frac{P_0}{\Delta p} = 1 + \frac{2\sigma_b}{R_0 \Delta p} \tag{2.9}$$

where P_0 is the partial pressure of the incondensible gas within the bubble at time $t = 0$.

3. Numerical implementation

Since we have potential flow in each fluid layer with $\nabla^2 \phi_i = 0$ for $i = 1, 2$ we base our numerical approach on the boundary integral method by using Green's function as will be detailed below. This allows us to examine the full flow field in our whole domain of interest by calculating the values of our potentials and their normal derivatives along the various bubble surfaces and the fluid–fluid interface. This reduces a fully three-dimensional problem to a two-dimensional problem. As noted in figure 3 we assume that the flow is axisymmetric. Therefore, a further reduction in complexity is gained, as the evaluation of the required Green's functions is reduced to the evaluation of complete elliptic integrals and the integration of the resultant kernels along curves parameterized by one variable.

We discretize our system by placing a finite number of nodes on our bubble surfaces and on the fluid–fluid interface with $\boldsymbol{b}$ representing a node on a bubble in fluid 1 and $\boldsymbol{p}$ representing a node on the fluid–fluid interface. The bubble surface and the fluid–fluid interface are then represented using quintic splines parameterized with respect to arclength with points $\boldsymbol{c}$ and $\boldsymbol{q}$ representing the interpolated values between nodes. The nodal points are advected according to

$$\frac{\mathrm{d}\boldsymbol{b}}{\mathrm{d}t} = \boldsymbol{u}_1(\boldsymbol{b}), \quad \frac{\mathrm{d}\boldsymbol{p}}{\mathrm{d}t} = (\boldsymbol{u}_1(\boldsymbol{p}) + \boldsymbol{u}_2(\boldsymbol{p}))/2. \tag{3.1}$$

When combined, equations (2.6)–(3.1) model the time evolution of our flow once we have determined our velocities $\boldsymbol{u}_1$ and $\boldsymbol{u}_2$. As detailed in Curtiss *et al.* (2013) these velocities are determined using the boundary integral method.

In particular in fluid 1 we have $\nabla^2 \phi_1 = 0$ in domain D_1 with boundary δD_1. Thus

$$c(\boldsymbol{x}_0)\phi_1(\boldsymbol{x}_0) = \int_{\partial D_1} \left(G(\boldsymbol{x}_0, \boldsymbol{x}) \frac{\partial \phi_1(\boldsymbol{x})}{\partial n} - \phi_1(\boldsymbol{x}) \frac{\partial G(\boldsymbol{x}_0, \boldsymbol{x})}{\partial n} \right) \mathrm{d}S \tag{3.2}$$

where $G(\boldsymbol{x}_0, \boldsymbol{x})$ is the free-space Green's function $1/|\boldsymbol{x} - \boldsymbol{x}_0|$ and $\partial G(\boldsymbol{x}_0, \boldsymbol{x})/\partial n$ is the normal derivative of the Green's function with respect to the outward normal of the fluid domain. All surfaces are smooth due to the spline interpolation, and as such all of the collocation coefficients are given as

$$c(\boldsymbol{x}_0 \in D_1 \backslash \partial D_1) = 4\pi, \tag{3.3}$$

$$c(\boldsymbol{x}_0 \in \partial D_1) = 2\pi. \tag{3.4}$$

Note that ∂D_1 includes the surfaces of the bubble in layer 1 and the fluid–fluid interface.

In the case where fluid 2 is of infinite depth (i.e. no solid boundary) the integral equation for ϕ_2 is identical to (3.2) with the subscript 1 everywhere replaced with a 2. When the solid boundary is present in fluid 2 we must modify our Green's function approach by defining an image point system with

$$G^2(\boldsymbol{x}_0, \boldsymbol{x}) = G(\boldsymbol{x}_0, \boldsymbol{x}) + G^{im}(\boldsymbol{x}_0, \boldsymbol{x}) \tag{3.5}$$

where

$$G^{im}(\boldsymbol{x}_0, \boldsymbol{x}) = \frac{1}{|\boldsymbol{x}_0 - (2H\boldsymbol{e}_z - \boldsymbol{x})|} \tag{3.6}$$

and $\boldsymbol{e}_z$ is the unit vector in the z direction of our cylindrical coordinate system. Thus, in fluid 2 we write

$$c(\boldsymbol{x}_0)\phi_2(\boldsymbol{x}_0) = \int\limits_{\partial D_2} \left(G^2(\boldsymbol{x}_0, \boldsymbol{x}) \frac{\partial \phi_2(\boldsymbol{x})}{\partial n} - \phi_2(\boldsymbol{x}) \frac{\partial G^2(\boldsymbol{x}_0, \boldsymbol{x})}{\partial n} \right) \mathrm{d}S. \tag{3.7}$$

Observe that $\partial G^2/\partial n = \partial \phi_2/\partial n = 0$ along the solid boundary at $z = H$. Hence, the surface integral in (3.7) is only evaluated along the density interface.

The procedures for discretizing (3.2) and (3.7) are detailed in Curtiss *et al.* (2013). For the case of a solid boundary in backing layer 2 and a pre-toroidal bubble in layer 1, the resultant equations are

$$\begin{bmatrix} G_{bc} & -G_{bq} & \dfrac{\rho}{1+\rho} DG_{bq} \\ G_{pc} & G^{im}_{pq} & \dfrac{\rho-1}{\rho+1} DG_{pq} - 2\pi I_{pq} - DG^{im}_{pq} \dfrac{1}{1+\rho} \\ G_{pc} & -2G_{pq} - G^{im}_{pq} & DG_{pq} + 2\pi \dfrac{1-\rho}{1+\rho} I_{pq} + DG^{im}_{pq} \dfrac{1}{1+\rho} \end{bmatrix} \begin{bmatrix} \dfrac{\partial \phi_1(b)}{\partial n_1} \\ \dfrac{\partial \phi_2(p)}{\partial n_1} \\ \phi_1(p) + \phi_2(p) \end{bmatrix}$$

$$= \begin{bmatrix} 2\pi I_{bc} + DG_{bc} & \dfrac{-1}{2+2\rho} DG_{bq} & G_{bq} \\ DG_{pc} & \dfrac{-1}{1+\rho} DG_{pq} - \dfrac{1}{2(1+\rho)} DG^{im}_{pq} & G_{pq} \\ DG_{pc} & 2\pi \dfrac{1}{1+\rho} I_{pq} + \dfrac{1}{2(1+\rho)} DG^{im}_{pq} & G_{pq} \end{bmatrix} \begin{bmatrix} \phi_1(b) \\ \phi_2(p) \\ F(p) \end{bmatrix}. \tag{3.8}$$

Here G refers to the discretized Green's function, DG refers to the discretized normal derivative of the Green's function and the block matrix structure and the subscripts indicate the bubble/bubble, bubble/interface and interface/interface contributions to the boundary integrals.

At each time step we can determine our nodal velocities by inverting (3.8) for the case of a solid backing plate (or the corresponding system given by Curtiss *et al.* (2013) for the case of no solid backing). Matrix inversion is done directly and without preconditioning. The relatively small number of nodes (at most 400 in these simulations) makes this viable. We can then integrate (2.6), (2.8) and (3.1) to update our nodal positions and potentials with respect to time. In practice fourth-order Runge–Kutta time stepping is used when the bubble dynamics are evolving rapidly. During relatively slow phases of the bubble dynamics second-order Runge–Kutta time stepping or even explicit Euler time stepping is used. The time step $\mathrm{d}t$ is adaptable, and is taken as a constant $\Delta\phi$ divided by the absolute maximum potential change on any bubble surface, or the absolute maximum change in the quantity F on the two-fluid interface. It should be noted that the incorporation of a vortex ring in the solid backing case to model toroidal bubbles follows directly from the procedure detailed by Curtiss *et al.* (2013) which is not repeated here.

Initial conditions

In this paper we consider the ultrasonic forcing of UCA bubbles. Dimensionally, we assume that our bubble is initially of radius $R_0 = 2.5$ μm and that it is in equilibrium

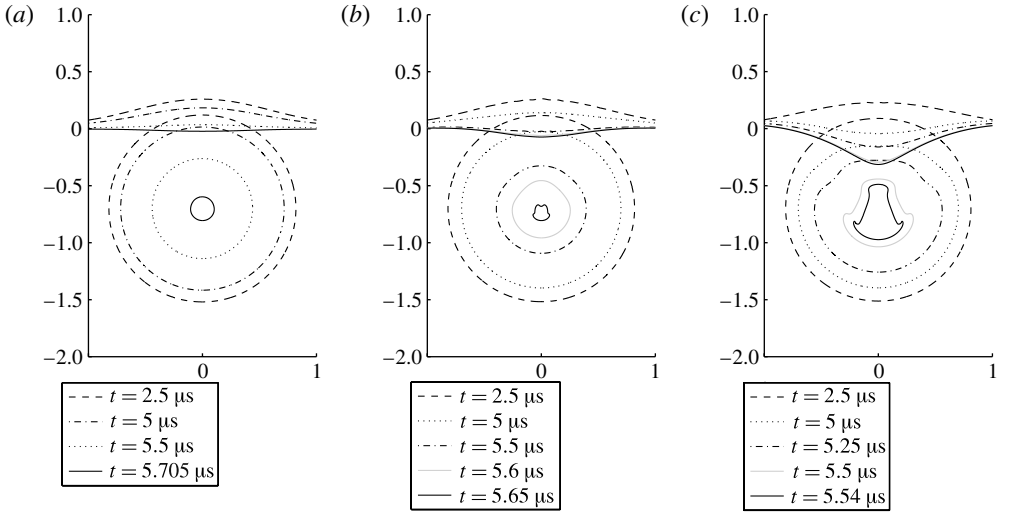

FIGURE 4. The effect of increasing the membrane tension through two non-dimensional orders of magnitude. The collapse phase for $h = 0.7$ is shown in each image at various different times: $\sigma_1 = 0.01$; $\sigma_1 = 0.1$; $\sigma_1 = 1$.

with the mean background pressure $\bar{p}$. We then use the Rayleigh–Plesset equation (equation (3.16) in Curtiss *et al.* (2013)) to determine the maximum radius that our bubble would obtain in an infinite fluid subject to the pressure forcing given by (2.5). This procedure gives us the value of R_{max} which is used in our non-dimensionalization. The values of surface tension along the bubble and the fluid–fluid interface are chosen to be typical of the biomedical applications of interest with the value of the density ratio ρ close to unity.

4. Membrane effects

We begin by investigating the effect of a membrane separating two types of tissue in the absence of a rigid backing plate. In this study various non-dimensional tension parameters are investigated, as the membrane tension present in biological structures may vary greatly.

To begin with consideration is given to the case $\rho = 1$. The effect of varying surface tension along the membrane through two orders of magnitude is investigated, with the standoff distance taken at the submaximum radius distance $h = 0.7$. The oscillatory far-field pressure term is given as $\tilde{p}_\infty = 1$ MPa with the driving frequency given as 0.2 MHz. This provides a maximum bubble radius of approximately 60 μm, with a collapse time of approximately 6 μs. Figure 4 shows the collapse from maximum volume with the non-dimensional interfacial tension varying through two orders of magnitude, $\sigma_I \in \{0.01, 0.1, 1\}$. These values correspond dimensionally to tensions of $6\sigma_I$ N m^{-1}. In the first case, the behaviour remains predominantly spherical throughout the collapse, implying this tension value promotes very little deviation from the tension-free case. For $\sigma_I = 0.1$ one sees non-spherical perturbations in the late collapse stage, resulting in an inverted mushroom-shaped bubble. Further increasing the tension to $\sigma_I = 1$ leads to the earlier onset of this disturbance, with mushroom shaping beginning shortly after maximum volume. The effect on the membrane is also clearly visible. The initial collapse of the bubble in collaboration with the membrane

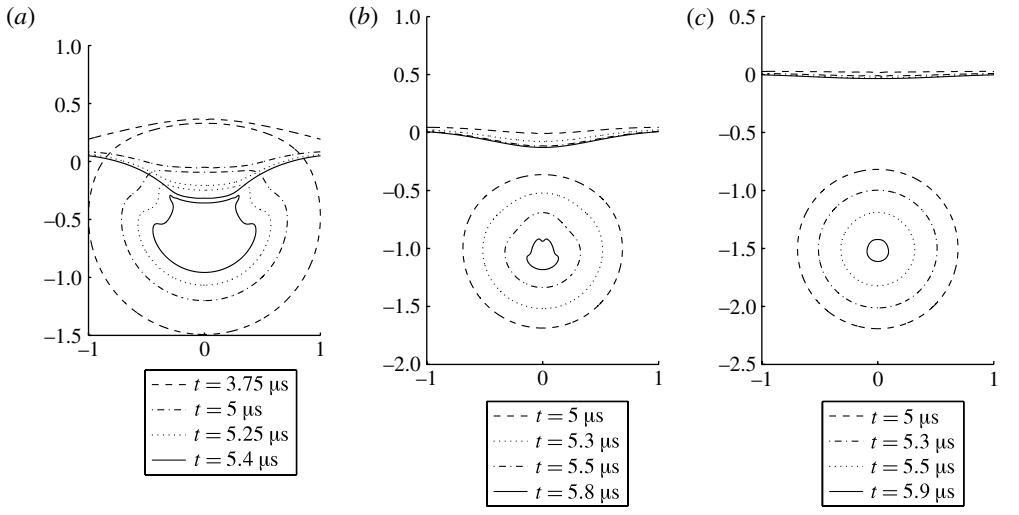

FIGURE 5. The Effect of standoff distance on membrane effects with a 2.5 μm bubble, driven by a standing acoustic wave with maximum amplitude 1 MPa and frequency 0.2 MHz, with the membrane tension of $\sigma_I = 1$: (*a*) $h = 0.5$, (*b*) $h = 1$; (*c*) $h = 1.5$.

tension drags the centre of the membrane downward, ending roughly 0.2 maximum bubble radii away from its rest position.

We now investigate the effect of standoff distance on this membrane behaviour, fixing the tension as $\sigma_I = 1$. This is shown in figure 5 for the standoff distances $h \in \{0.5, 1, 1.5\}$. At the greatest of these, $h = 1.5$, the membrane effect is heavily diminished. The bubble remains almost spherical throughout, developing only slight perturbations toward the end of the collapse. The membrane itself returns to a near-flat position at the end of the oscillation. Such behaviour is very different from what we observed when varying the density ratio in Leppinen *et al.* (2011), where for all of the values of ρ tested at this standoff distance distinctive jetting was seen to occur. Decreasing the standoff distance by half a maximum bubble radius to $h = 1$, induces more significant perturbations. During the collapse phase there is some flattening of the near side of the cavity, which results in the development of a mushroom-shaped bubble. Late in the collapse a further indentation forms on the nearer side of the bubble to the interface. The interface is more heavily perturbed, with a downward hump formed through the rebound from the earlier peak deformation. At the close standoff distance $h = 0.5$ very significant differences become apparent. The bubble expansion is retarded by the membrane, resulting in a flatter surface hump. Upon collapse, the interface remains close to the bubble. The two surfaces are however separated by a thin layer of fluid, and in this potential model do not come into contact. The bubble forms a horizontal indentation near to the interface, resulting in the severe shape perturbation at a large volume. The proximity of the rebounding interface forces the top of the bubble into a concave shape. A second indentation forms in a more horizontal direction and grows vertically along the edge of the bubble. This is unlike any of the behaviour yet seen in this work. It is however reminiscent of the experimental results in Brujan *et al.* (2001*a*,*b*) of laser bubble behaviour near an elastic boundary, and in qualitative agreement with the numerical and experimental result of Turangan *et al.* (2006), using high-pressure spark-generated bubbles near a

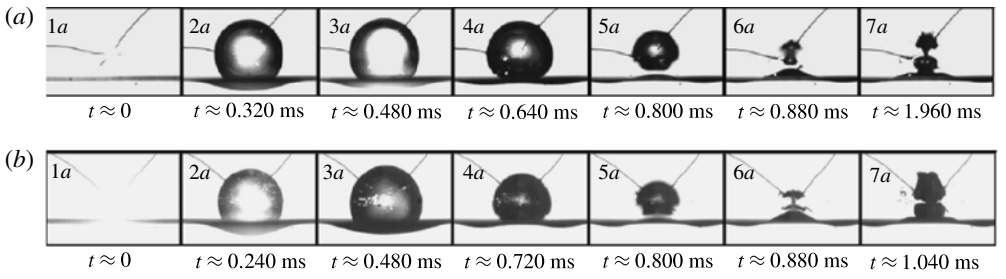

FIGURE 6. Experimental behaviour near a thin elastic membrane submerged in water with a tension of 43.6 N m^{-1}, for standoff distances $h = 0.55$ (*a*) and $h = 0.7$ (*b*) taken from Turangan *et al.* (2006). The bubbles are formed through spark discharge, with a maximum radius $R_{max} \approx 3.3$ mm.

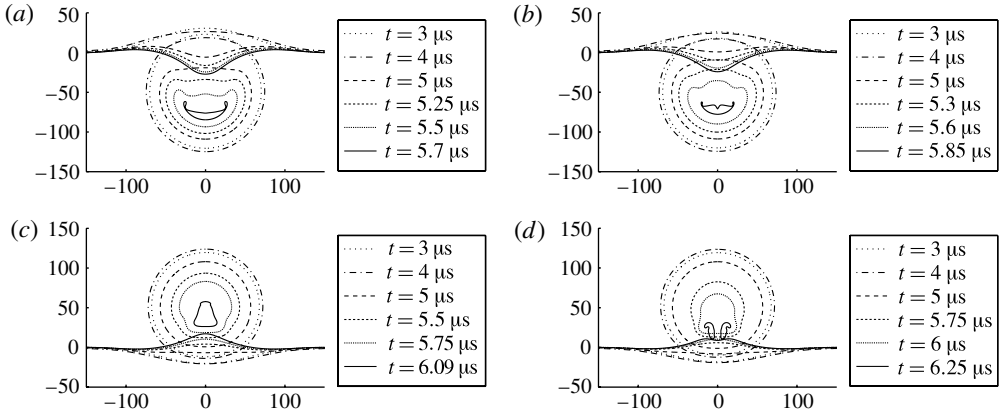

FIGURE 7. Bubble and surface shapes associated with acoustic driving with a frequency of 0.2 MHz, and a peak pressure of $\tilde{p}_\infty = 1.4$ MPa, with unit non-dimensional membrane tension: (*a*) $\rho = 0.6$; (*b*) $\rho = 0.8$; (*c*) $\rho = 1.2$; (*d*) $\rho = 1.4$.

thin elastic membrane with a tension of 43.6 N m^{-1}. Some examples from the latter are shown in figure 6, for bubbles initiated at standoff distances of $h = 0.55$ and $h = 0.7$.

It is also important to investigate whether the membrane can affect the dynamics associated with the variation of the density ratio. In particular, it is of significant interest as to whether the direction of any bubble jetting induced by the density variation will be affected. Figure 7 contains four simulations for the density ratios $\rho \in \{0.6, 0.8, 1.2, 1.4\}$, with the fluid–fluid interface supporting unit non-dimensional tension. For the subunity density ratios, one still observes the repulsive effect of the density discontinuity. In each case a very broad downward jet forms, which results in a non-axial impact. This is in stark contrast to the equal fluid case, where no jet formation is seen at a comparable time. The interface itself rebounds heavily in both cases, ending approximately 25 μm from the initial location. This is in good agreement with the deflection observed for the unity density case.

The cases where $\rho > 1$ still show attraction toward the denser layer. The associated bubble dynamics illustrate the formation of an indentation on the near side of the

bubble, giving the cavity a distinctive mushroom shape. The presence of the density jump then causes the larger far side of the bubble to collapse inwards as in the close standoff simulations presented by Leppinen *et al.* (2011), which results in a fatter region near the interface. This is the opposite of the behaviour observed for $\rho = 1$ at this standoff distance. The interface behaves in a similar manner to the previous simulations, with a significant rebound toward the bubble. This may itself act as an accelerant to the subsequent jetting behaviour, which is still directed toward the interface. This is clearly seen for the case $\rho = 1.4$, the density of cornea (Fong *et al.* 2006). The force of the impacting liquid jet is also sufficient to deflect the rebounded membrane, which will lead to further elastic wave propagation along the interface. This is significant for cell permeation techniques, as it shows the rebound of the membrane is not necessarily sufficient to reverse the jet direction, and may in fact enhance the damaging mechanism further.

5. The influence of rigid backing

The interaction of a bubble with a density interface can be significantly altered by the surrounding geometry. Here, we introduce a backing solid behind the second liquid layer. One may envision this as a model for sonoporation near a cell layer attached to a bone. Furthermore, this is indeed the situation in many *in vitro* experiments where a solid plate is used to mount a specimen, as in the investigations of Prentice *et al.* (2005) into UCA-assisted sonoporation, for example. *In vivo* there may be microcavities present inside the cell layer, which will be activated by the pressure fluctuation. However, these are assumed to be inconsequential in comparison with the dynamics induced by the primary UCAs. This assumption is made, as the necessary contaminant gas pockets are likely to be on the order of nanometres, whereas the UCAs are on the order of micrometres and so will expand to a significantly larger size.

5.1. *Membrane peeling at submegahertz frequencies*

A particularly interesting feature discovered in this research is the removal of the ‘tissue’, or ‘cell’, layer from the substrate through the toroidal action and re-expansion of the cavitation bubble or UCA. This behaviour is referred to here as membrane peeling.

To begin one examines the system governed by $\rho = 1$, under the influence of an acoustic wave with a frequency of 0.2 MHz and a maximum amplitude of $\tilde{p}_\infty = 1.4$ MPa. The rigid boundary is located at a dimensional distance of $H = 25$ μm from the two-fluid interface, roughly corresponding to a non-dimensional distance of 0.34 maximum bubble radii. The tension on the interfaces is of low order, and so it will not significantly affect the simulation. The model therefore is very close to the collapse of a bubble in an infinite fluid near to a rigid boundary, albeit in the presence of a membrane with little tension. Figure 8 shows the associated bubble behaviour as the standoff distance is varied through $h \in \{0.5, 0.75, 1, 1.25\}$ during the later stages of collapse, and the complete simulation of the case $h = 0.75$ is shown in figure 9 for clarity. For the larger standoff distance, one observes the formation and expansion of the bubble toroid, resulting in the forward lobe. This is seen to close at the tip as the bubble continues to evolve. At the closer standoff distances, the toroidal bubble interacts with the wall, resulting in the forward lobes being forced outward radially. Consequently, the bubble jet will not pinch off as rapidly as the bubble re-expands. The fluid–fluid interface in these cases is initially compressed against the wall in the

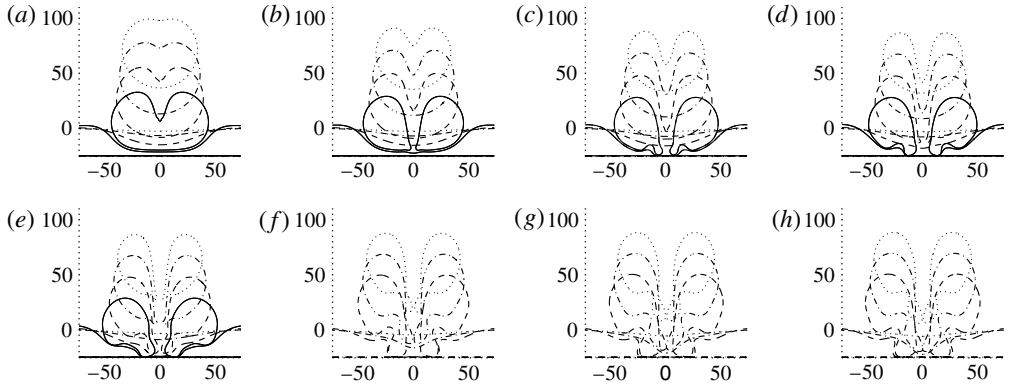

FIGURE 8. Toroidal bubble action near a cell layer of depth $H = 25$ μm and relative density $\rho = 1$, due to a 2.5 μm microcavity excited by an acoustic wave with a frequency of 0.2 MHz and a maximum amplitude of $\tilde{p}_\infty = 1.4$ MPa: (*a*) $t = 6.3002$; (*b*) $t = 6.5001$; (*c*) $t = 6.65$; (*d*) $t = 6.8009$; (*e*) $t = 7.0006$; (*f*) $t = 7.3012$; (*g*) $t = 7.4005$; (*h*) $t = 7.4301$. Bubble initiation is at $h = 0.5$ (solid), $h = 0.75$ (dashed), $h = 1$ (dot-dashed) and $h = 1.25$ (dotted).

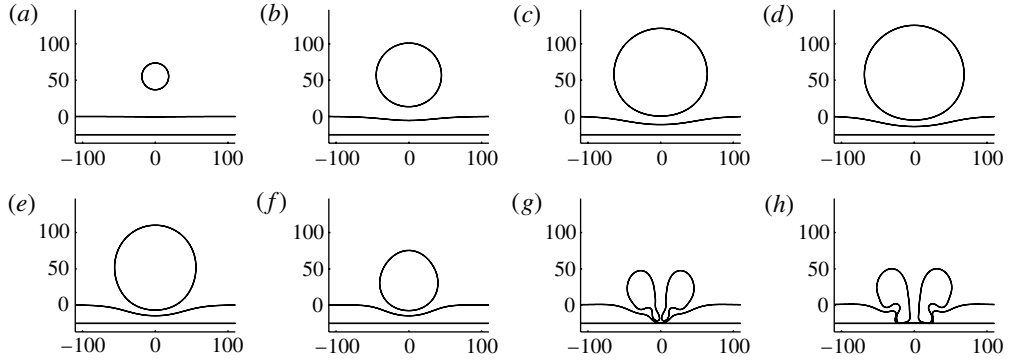

FIGURE 9. The lifetime of a bubble initiated at $h \approx 50$ μm to a cell layer of depth $H = 25$ μm and relative density $\rho = 1$: (*a*) $t = 1.0018$; (*b*) $t = 2.0184$; (*c*) $t = 3.0059$; (*d*) $t = 4.0071$; (*e*) $t = 5.0215$; (*f*) $t = 6.0007$; (*g*) $t = 7.0012$; (*h*) $t = 7.4005$. The bubble is activated by an ultrasound wave with a frequency of 0.2 MHz, and a maximum pressure of $\tilde{p}_\infty = 1.4$ MPa.

region directly below the mouth of the liquid jet. The re-expansion of the forward toroidal lobes then cuts underneath the interface, lifting the fluid in the second layer away from the substrate. It is this interaction that one describes as membrane peeling.

This presents a significant new mechanism for tissue damage. Circumstantial evidence may be visible in the cornea specimen micrograph in figure 1 created by Vogel *et al.* (1990). Here a large area with a radius of approximately 100 μm surrounding the jet impact location has been scraped away. Previous work has postulated that this is due to the shear stress caused by the high fluid velocity beneath the bubble. This membrane peeling may however provide an additional mechanism, associated with the re-expansion of the toroidal bubble.

Varying the membrane tension may provide a better approximation to a biological tissue. Importantly, it will show whether the bulk fluid motion is a result of the

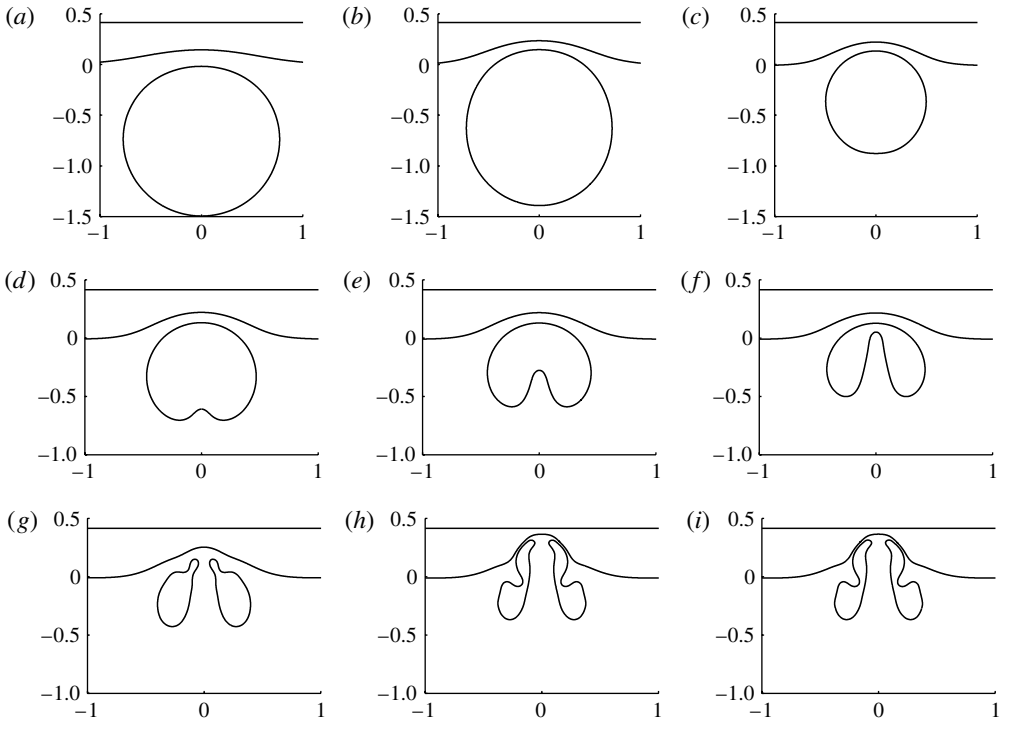

FIGURE 10. Shapes from the simulation of a bubble driven by an acoustic wave with frequency 0.2 MHz and peak pressure $\tilde{p}_\infty = 1$ MPa: (*a*) $t = 2.5045$ μs; (*b*) $t = 5.0254$ μs; (*c*) $t = 5.7002$ μs; (*d*) $t = 5.8002$ μs; (*e*) $t = 5.9$ μs; (*f*) $t = 6.0001$ μs; (*g*) $t = 6.1004$ μs; (*h*) $t = 6.2006$ μs; (*i*) $t = 6.2013$ μs. The parameters of the flow field are $H = 25$ μm, $\rho = 1$ and $h = 1 \approx 60$ μm. The membrane has zero interfacial tension, $\sigma_I = 0$.

inclusion of the rigid boundary, or the influence of the membrane. Figures 10 and 11 show simulations using a 0.2 MHz acoustic wave with maximum amplitude $\tilde{p}_\infty = 1$ MPa at a standoff distance of $h = 1 \approx 60$ μm. The surface tension on the bubble surfaces is $\sigma_b = 0.00165$ to model the effect of a UCA, and the membrane tensions used are $\sigma_I = 0, 1$ respectively. The backing plate is again located at $H = 25$ μm dimensionally. The shapes in the zero tension case naturally agrees with a single layer of fluid with $h \approx 1.35$, as did the simulation shown in figure 9. The bubble toroid forms as normal, with the advancing jet and lobe forcing the interface against the backing plate. The inclusion of unit membrane tension significantly inhibits this behaviour. The rebounded interface causes the near-boundary side of the interface to flatten in comparison to the rounded shape observed in its absence. The bubble forms a jet directed toward the interface, in contrast to the behaviour of a bubble near a floating membrane with the same tension. As the toroid forms, the circular disturbance is initially forced outwards. The jet forms a wide pit in the tissue layer, and the advancing bubble then slides in along the sides of the pit.

The pressure and velocity fields associated with this injection into the tissue layer can be seen in figure 12, with the frames taken at dimensional times 5.9 μs, 5.95 μs and 6.0 μs. Owing to the frequency examined here, these occur roughly 1 μ s after a complete acoustic cycle. The pressure applied by the sound wave is approximately −0.95 MPa, approaching the second pressure minimum. The pressures observed near

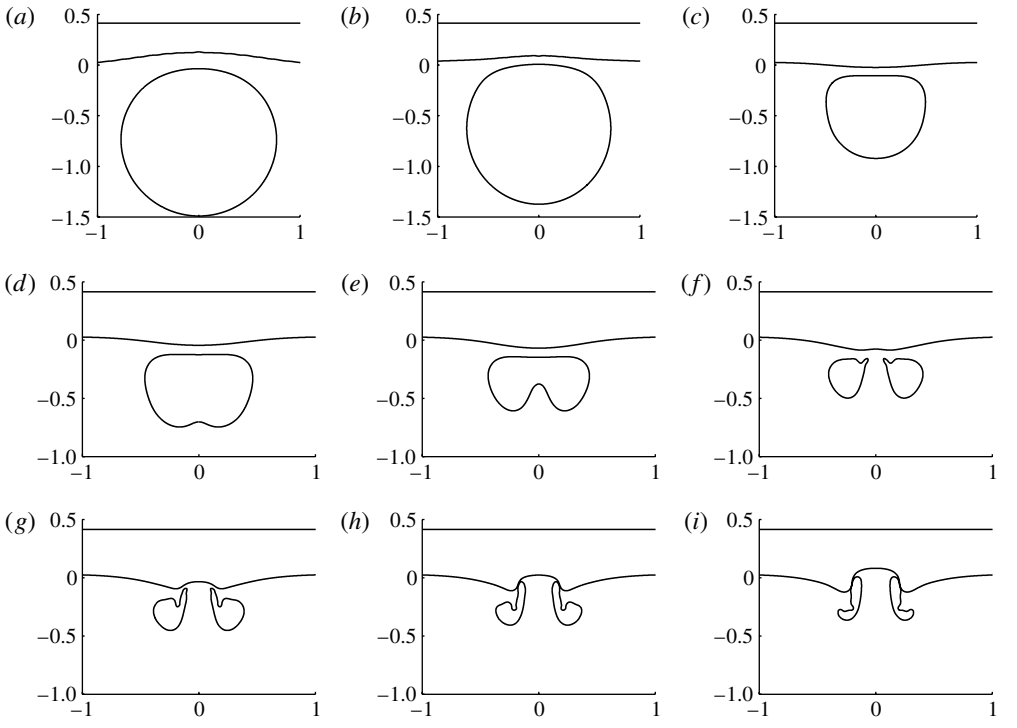

FIGURE 11. Shapes from the simulation of a bubble driven by an acoustic wave with frequency 0.2 MHz and peak pressure $\tilde{p}_\infty = 1$ MPa: (*a*) $t = 2.5008$ μs; (*b*) $t = 5.0037$ μs; (*c*) $t = 5.6023$ μs; (*d*) $t = 5.701$ μs; (*e*) $t = 5.8007$ s; (*f*) $t = 5.9006$ μs; (*g*) $t = 5.9501$ μs; (*h*) $t = 6.0004$ μs; (*i*) $t = 6.0507$ μs. The parameters of the flow field are $H = 25$ μm, $\rho = 1$, $h = 1 \approx 60$ μm. The membrane has unit interfacial tension, $\sigma_I = 1$.

the impact zone however far outweigh this, being over 10 MPa just after toroidal formation, although the pressure inside the second layer falls as the bubble re-expands. Before the toroidal phase, the liquid in the cell layer is flowing toward the cavitated layer to some extent, with a somewhat axial direction. After impact, this causes a point of zero velocity to form on the axis below the jet, which rapidly translates toward the wall. One then observes the translation of a stagnation point along the rigid boundary, with fluid forced radially outward by the jet being deflected toward the cavitated layer by the axially directed flow resultant of the bubble compression. The high pressure region focused at the impact site also dissipates outwards as the bubble jet continues to penetrate. These factors force the fluid near the forward bubble lobe to flow upward, exacerbating the height of the jet pit wall.

As in the floating membrane cases, one seeks to assess the effect of varying the density ratio. The following simulations were driven by a standing acoustic wave with peak pressure $\tilde{p}_\infty = 1.4$ MPa and a frequency of 0.2 MHz. The cell layer depth is $H = 25$ μm, with the standoff distance fixed at $h = 1$, approximately 73 μm. The dimensionless bubble surface tension and interfacial tension are $\sigma_b = 0.01$ and $\sigma_I = 1$, respectively. The bubble surface tension acts to inhibit the leading edge of the toroid from rejoining, allowing the simulation to proceed further and, hence, to increase the calculated peeling effects. This is more representative of a UCA than the case with zero surface tension. The extent of peeling for density ratios $\rho \in \{0.8, 0.9, 1.1, 1.2\}$ is

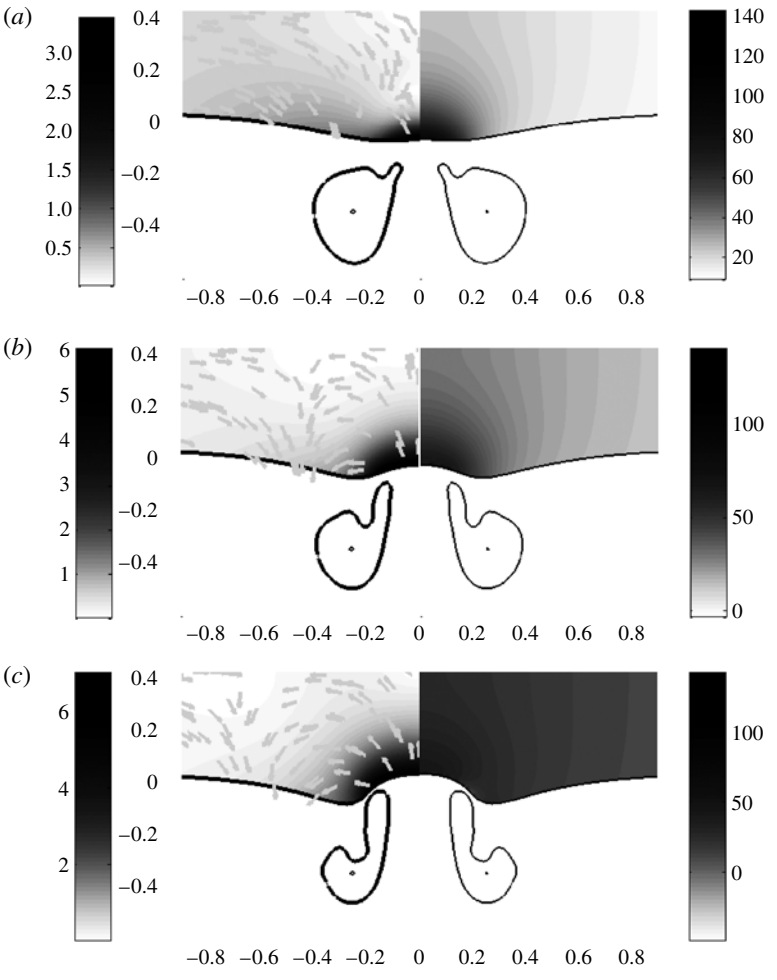

FIGURE 12. Pressure and velocity in the cell layer after bubble jet impact has occurred for $\tilde{p}_\infty = 1$ MPa, frequency $= 0.2$ MHz, $H = 25$ μm, $\rho = 1$ and $h = 1 \approx 60$ μm. The membrane has unit interfacial tension. Dimensional times are 5.9 μs (*a*), 5.95 μs (*b*) and 6.0 μs (*c*).

shown in figure 13 for the same time frame. In all cases the under cutting of the cell layer is visible. The bubble shapes show some variation, although all form the same general 'C' shaped structure in the r, z plane, with the density ratios furthest from unity showing slightly more peeling. However, this does not appear significant, and so we conclude that there is little variation in peeling for density ratios close to 1.

5.2. *Backed behaviour at 1 MHz*

In the previous examples, the submegahertz frequency allowed the cavity to expand greatly, to a radius much larger than the typical dimensions of a cell. Indeed the peeling observed in figure 13 was over a region with radius approximately 40 μm, four times the size of a typical eukaryotic cell, and would have continued significantly further as the bubble re-expanded. At megahertz frequencies, however, the bubble expansion is restricted, and as such it is unclear whether the peeling behaviour is still observed, given that surface tension in particular will have a more significant

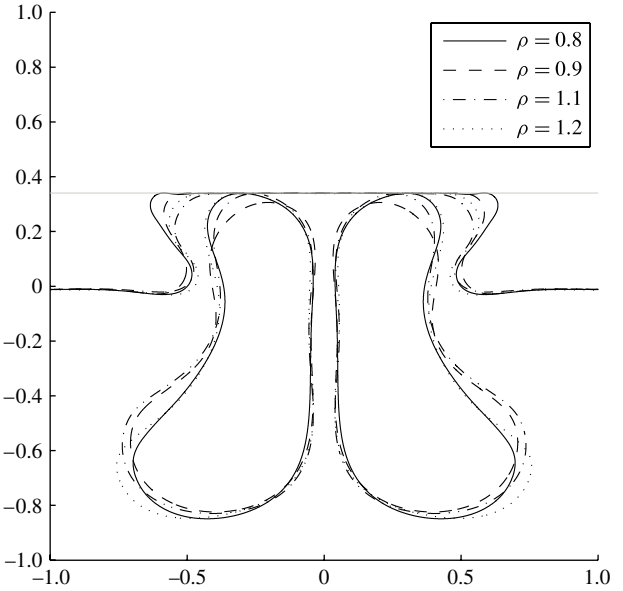

FIGURE 13. Comparison between bubble and interface shapes as ρ is varied near unity under identical acoustic forcing, surface tension and standoff distances. The depth of the second layer is dimensionally $H = 25$ μm.

effect. In addition, with this restricted maximum bubble radius, it is now reasonable to investigate varying the depth of the cell layer, as the maximum radii is of the order of the size of a eukaryotic cell.

We consider the case of a UCA bubble with $R_0 = 2.5$ μm and dimensional surface tension $\sigma_b = 51$ dyn cm^{-1} representative of a Sonovue UCA (Marmottant *et al.* 2005). The bubble is driven by an ultrasonic wave with a frequency of 1 MHz and a peak pressure 1 MPa. This results in a maximum bubble radius of $R_{max} = 13.18$ μm. A standoff distance of $h_{dim} = 9.881$ μm is chosen, corresponding to the non-dimensional standoff distance $h = 0.75$. As was seen previously, the density of the cell layer does not have a significant effect on this phenomena, and as such the density ratio $\rho = 1$ is taken. The membrane is loaded with a tension of 0.5 dyn cm^{-1}.

The first simulation in this regime is shown in figures 14 and 15, illustrating the pre- and post-toroidal phases of the collapse, respectively. The pressure fields in both graphs do not include the pressure wave, and as such show the pressure exerted by the collapsing bubble only. The first frame in the pre-toroidal figure is taken near the maximum radius of the bubble, at the start of the first collapse. Interestingly a stagnation point is clearly visible along the wall in the second fluid layer, as fluid is still being forced outwards by the advancing bubble front, whilst the fluid in the far field is being sucked back in toward the centre. Minimum pressures are around 1 MPa so the total pressure will be near equilibrium about the bubble, and between the bubble and the wall. As the collapse continues one observes the removal of the stagnation point, as the bubble contracts sucking water inward. The inevitable high-pressure region begins to form behind the bubble and will drive the subsequent jet toward the cell layer. The interface itself remains similarly disturbed about the axis, whilst it has recovered toward the initial position elsewhere. As jetting begins, the bubble is rapidly

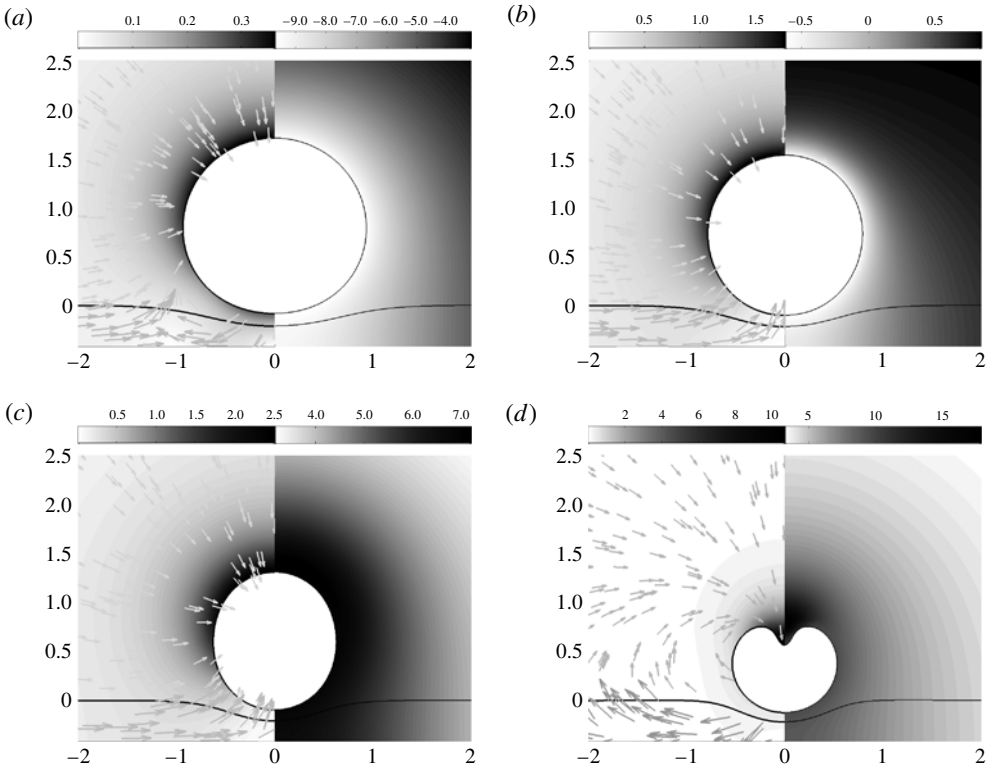

FIGURE 14. Speed and velocity (*a,c*) and pressure (*b,d*) fields during the pre-toroidal phase for a UCA undergoing a forcing of $\tilde{p}_\infty = 1MPa$ at a frequency of 1 MHz, at an initial standoff distance $h = 0.75$ and with a rigid wall located at $H = 0.42$: $t = 0.6$ (*a*); $t = 0.76$ (*b*); $t = 0.85$ (*c*); $t = 0.99$ (*d*). The UCA has surface tension $\sigma_b = 51$ dyn cm^{-1}, whilst the membrane separating two equal density layers has tension $\sigma_I = 0.5$ dyn cm^{-1}.

moving toward the wall, and as expected liquid is being forced into the jet at high velocity. Jet tip speeds for this case were of the order of 10 non-dimensional units, corresponding to $\sim$100 m s^{-1} and, thus, subsonic.

At impact, a peak pressure of approximately 40 atmospheres is exerted in the near vicinity. This acts to accelerate the fluid below the bubble away, and causes a distinct deformation of the interface. The bubble then begins to expand, and a stagnation point forms behind the bubble jet. The jet velocity itself is slowed to around 6 non-dimensional units at the fastest point. The high-pressure decreases and becomes more focused at the axis near the wall, forcing fluid sideways. The forward lobe of the toroidal bubble expands downward, until the wall prohibits any further advancement. This acts to prohibit fluid escaping the base of the jet, which re-increases the pressure at the jet tip to approximately 40 atmospheres. The bubble lobes are forced outward along the wall, and begin to undercut the separated layer. As the process continues, the membrane becomes entrained into the fluid pocket between the two bubble lobes. The pressure drops near the wall as the jet base expands, and a region of higher pressure is observed to form on the other side of the toroidal bubble in the cell layer. Hence, the peeling motion is again observed in this parameter regime, albeit at a smaller length scale than above.

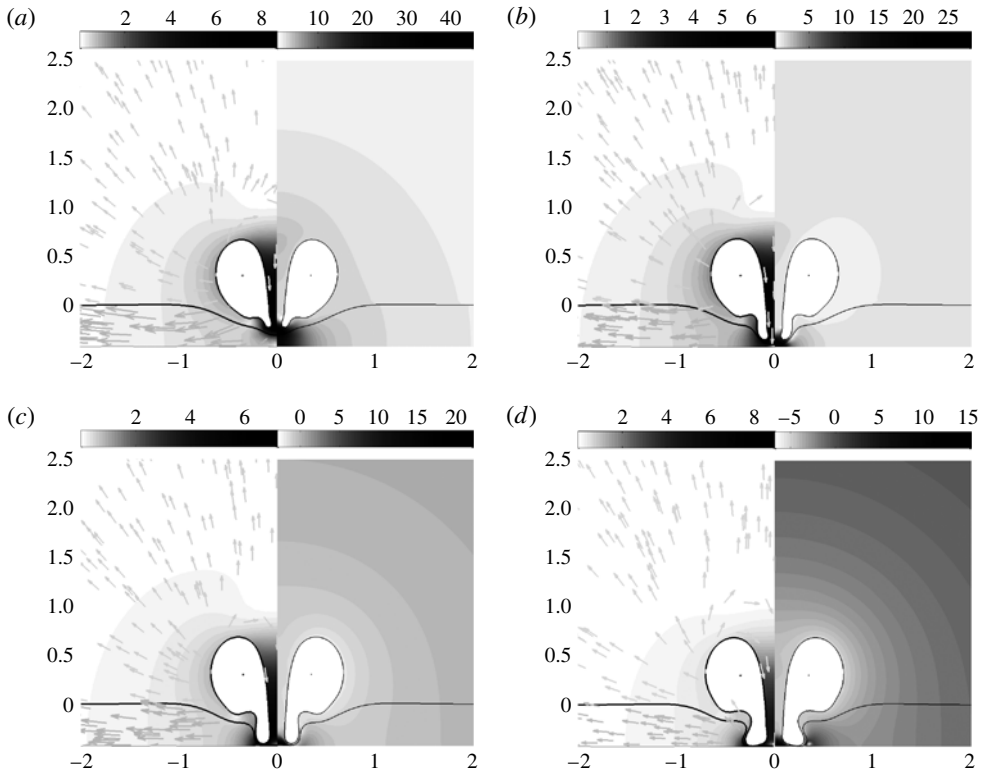

FIGURE 15. Speed and velocity (*a,c*) and pressure (*b,d*) fields during the post-toroidal phase for a UCA undergoing a forcing of $\tilde{p}_\infty = 1MPa$ at a frequency of 1 MHz, at an initial standoff distance $h = 0.75$ with a rigid wall located at $H = 0.42$: $t = 1.1$ (*a*); $t = 1.13$ (*b*); $t = 1.16$ (*c*); $t = 1.20$ (*d*). The UCA has surface tension $\sigma_b = 51$ dyn cm^{-1}, whilst the membrane separating two equal density layers has tension $\sigma_I = 0.5$ dyn cm^{-1}.

Decreasing the layer depth creates some distinct differences in the peeling behaviour. Figures 16 and 17 contain bubble shapes and pressure and velocity fields, respectively, for the case $H = 0.2$, with time frames beginning just after jet impact and continuing through the development of the forward bubble lobe. Impact occurs at a distance of approximately 0.1 maximum bubble radii from the wall and at half the initial depth of the second layer. Significantly high pressures are observed about the impact site, of the order of 100 atmospheres, and well above the driving pressure $\tilde{p}_\infty$. Jet velocities are in excess of 12 non-dimensional units about this region, and are rapidly slowed to below 6 by the near-stationary fluid in front of the jet. From the velocity directional arrows, it can be seen that at this point the bubble is already expanding, with fluid being forced outward along the lower layer, with the fluid in the primary layer being driven around the toroid. A stagnation point has formed at approximately 1.2 maximum bubble radii away from the initial level of the interface, although this appears to have little effect on the quantity of liquid entering the bubble jet. As time advances 0.2 non-dimensional units, the pressure about the impact point lessens significantly toward a maximum of 55 atmospheres at the end of the jet next to the rigid boundary. By this time the interface has been forced flat against the wall over a radius of 0.1 maximum bubble radii. The velocity of the jet has decreased somewhat, with the rest of the

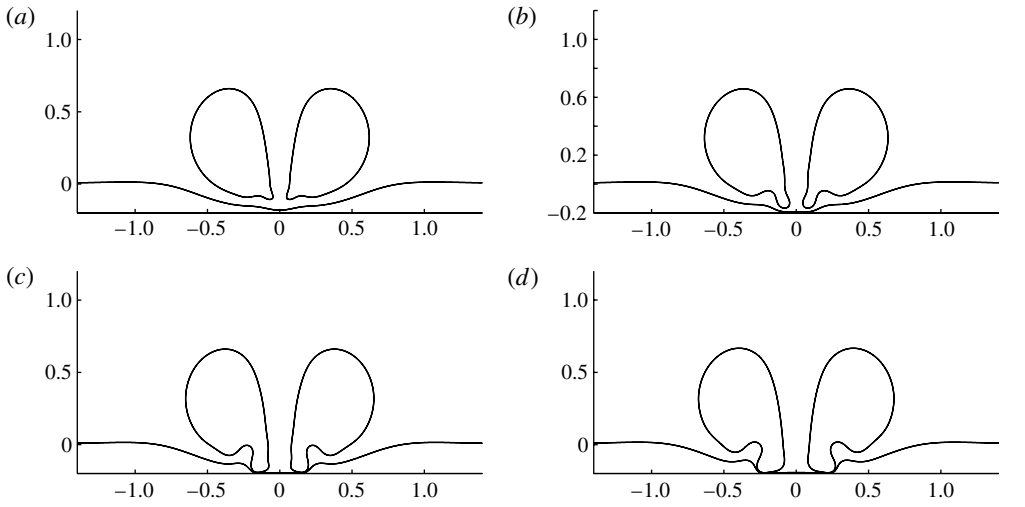

FIGURE 16. Bubble shapes during the toroidal phase of a UCA collapse near a backed liquid layer: (*a*) $t = 1.3801$ μs; (*b*) $t = 1.4$ μs; (*c*) $t = 1.4202$ μs; (*d*) $t = 1.4501$ μs. The dimensional simulation parameters are $R_0 = 2.5$ μm, $\sigma_b = 51$ dyn cm^{-1}, $\sigma_I = 0.5$ dyn cm^{-1}, $\rho = 1$, $\tilde{p}_\infty =$ 1 MPa with the acoustic wave driven at a frequency of 1 MHz. The non-dimensional standoff distance from the interface is $h = 0.75$, with the depth of the second layer $H = 0.2$.

field still exhibiting the same flow properties. Advancing time by a further 0.1 non-dimensional units presents the beginning of the peeling motion. The advanced ring of the toroidal bubble has been arrested by the presence of the wall and the outer ring jet has begun to form, forcing fluid upward and toward the central jet. The pressure has again dropped, with the maximum pressure occurring inside the fluid pocket generated by the advancing bubble lobe and the wall. Maximum pressure is now approximately 40 atmospheres, still greatly in excess of the driving amplitude. A region of pressure at ∼20 atmospheres has also formed directly below the secondary jet ring. At the end of the simulation, the peeling effect can clearly be seen. The forward lobe has forced the second layer to a near-vertical position as the bubble has further re-expanded. The pressure now observed has massively increased toward 160 atmospheres on the outside of the bubble in the lower layer, demonstrating that damage may continue to be caused well after jet impact. The velocity field also illustrates the rolling motion of the secondary ring jet about the toroid, with fluid moving upward toward the bubble centre at a significant velocity. In addition, the stagnation point has also translated downward to 1 bubble radii above the initial interface position, while the maximum jet velocity has decreased to 6 non-dimensional units. It would be reasonable to assume that significant damage would be caused to a tissue layer in this configuration through inertia alone.

Increasing the cell layer depth generates drastically different behaviour. This is first demonstrated in figures 18 and 19, containing the pre- and post-jet impact fluid motion and pressure fields for $H = 1.6R_{max}$. At maximum bubble radius the bubble and flow field exhibit the usual characteristics. The shape is roughly spherical, with the near pressure increasing in a uniform radial manner. Toward the wall fluid is naturally advected away from the axis, although the fluid velocity is near zero. As the bubble collapses, the classical higher pressure region above the bubble may be seen, with the fluid moving slightly faster in this region. As the jet forms, one observes the liquid in

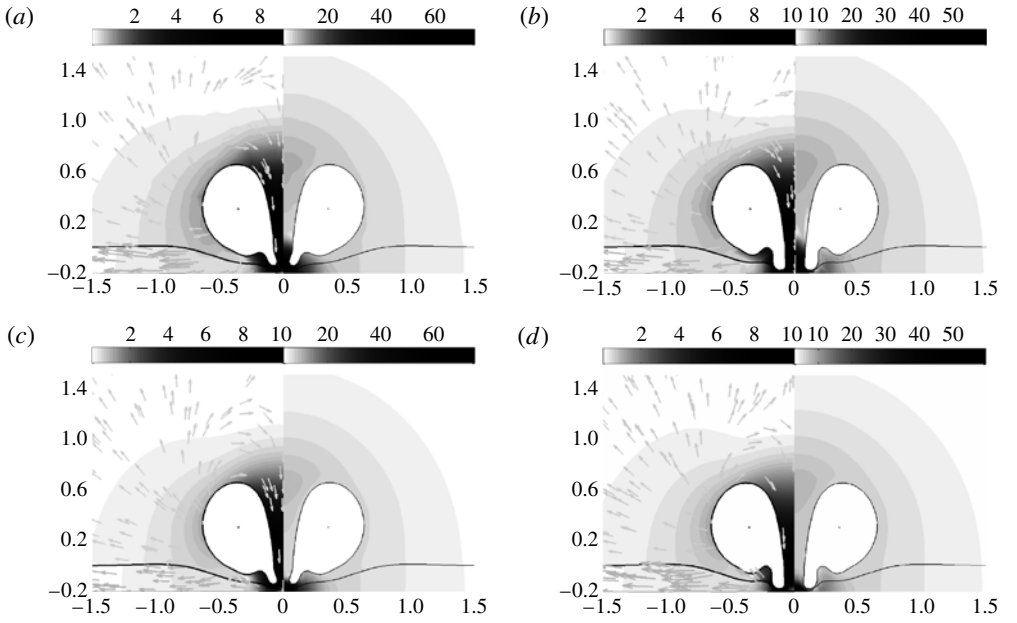

FIGURE 17. Velocity and pressure fields for a bubble as characterized in figure 16, during the toroidal phase with layer thickness $H = 0.2R_{max}$: $t = 1.04$ (a); $t = 1.06$ (b); $t = 1.08$ (c); $t = 1.11$ (d).

the primary layer being driven about the bubble and into the jet, with the formation of a stagnation point above the bubble at approximately $2.25R_{max}$. By this point the bubble centroid has migrated approximately $0.25R_{max}$ toward the interface and the wall, whilst the interface has returned toward being flat.

The most significant differences occur during the toroidal phase. Firstly, the pressures around the jet impact site are significantly lower. This is due to the presence of a much thinner jet, caused in part by the rapid migration of the over bubble stagnation point to a position of 1, restricting fluid flow into the jet. The increased depth also allows for the pressure to dissipate more before the wall. As this phase continues, the advance of the forward lobe is not arrested by the rigid boundary, and continues to drive the interface downwards as the bubble begins to collapse. The stagnation point also disappears, allowing more liquid to flow through the toroid. The advance of the bubble is slowed by the fluid flowing upward in the lower layer due to the bubble volume compression, and which is itself deflected around the forward bubble ring. The higher-pressure region about the impact site dissipates greatly, almost to equilibrium with the surrounding pressures. As the simulation continues, one observes the fluid in the lower layer flowing around the tip and back in toward the axis, causing the bubble to pinch and the interface to create an overhang. At the rear of the bubble a high-pressure ring forms, creating a secondary jetting motion about a torus. Velocities about this jet are comparably high to the initial jet, being of magnitude approximately 8. It is reasonable to expect that this ring jet will cause less damage to the tissue layer than the first, as it is effectively from a smaller bubble. The tissue layer itself has returned to its initial position over $r > 0.6R_{max}$, a significantly larger area than achieved in the closer collapses. This type of behaviour may be more beneficial for drug injection, as less damage to the cell layer appears to have occurred.

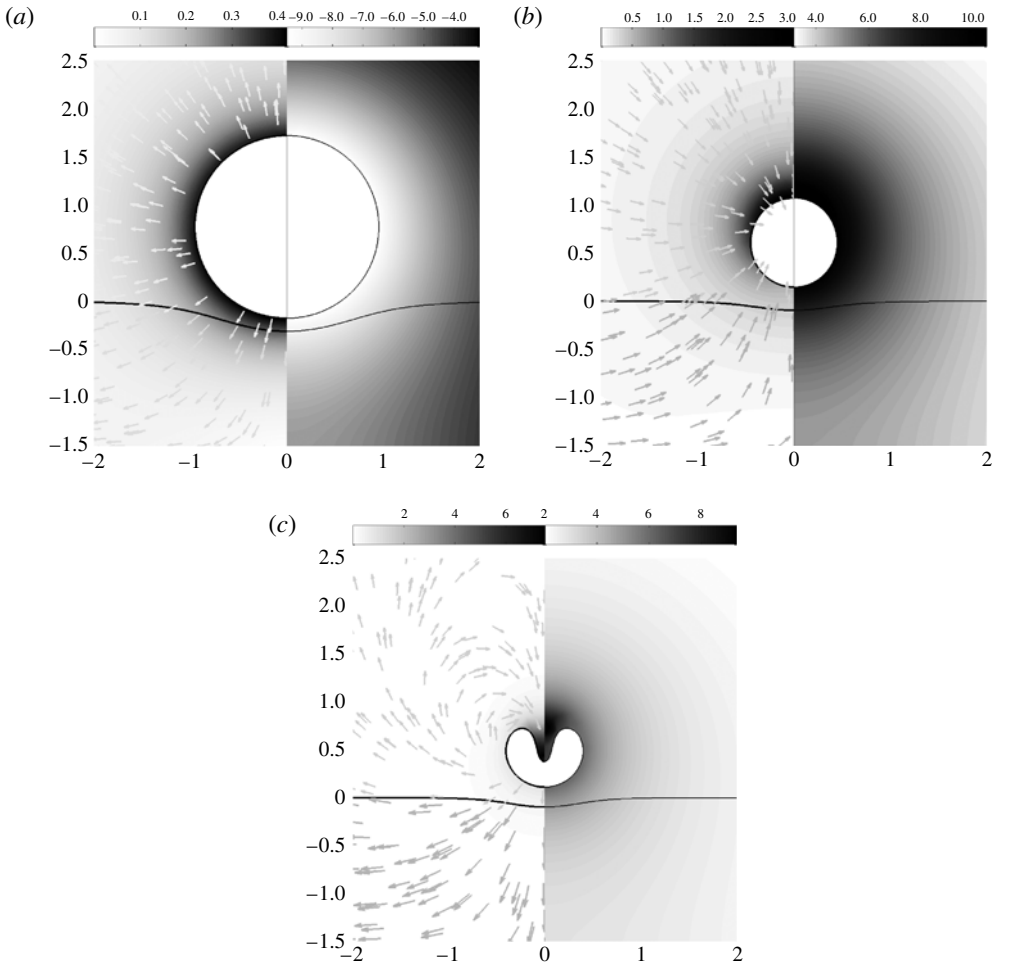

FIGURE 18. Pre-toroidal flow fields for an acoustically driven cavitation bubble with identical parameters to figure 15, with a rigid wall located at $H = 1.6R_{max}$ from the initially flat interface: $t = 0.532$ (*a*); $t = 0.95$ (*b*); $t = 1.06$ (*c*).

In addition, the forward bubble lobe may break off, with the interface potentially reforming above it, literally injecting a section of the bubble into the tissue. This is very different from the thin layer cases, where the section of bubble connecting the two lobes remained reasonably broad.

Increasing the layer depth further to $H = 2.0$ maximum bubble radii produces similar results. One may see this in figure 20 at non-dimensional times $t = 1.178$, 1.216 and 1.299. The first of these frames occurs after jet impact, with a developed forward lobe. At this time fluid in the region of the interface is flowing nearly parallel to it. The pressure spike formed by the jet impact has diminished somewhat, yet is still clearly visible. The second frame is taken shortly before the over pressure reaches its maximum. In contrast to the first frame, the fluid flow is now perpendicular to the interface, and there is a substantial movement of liquid toward the top of the threading jet. Fluid in the lower layer is still moving away from the bubble, indicating the bubble is still expanding at this point.

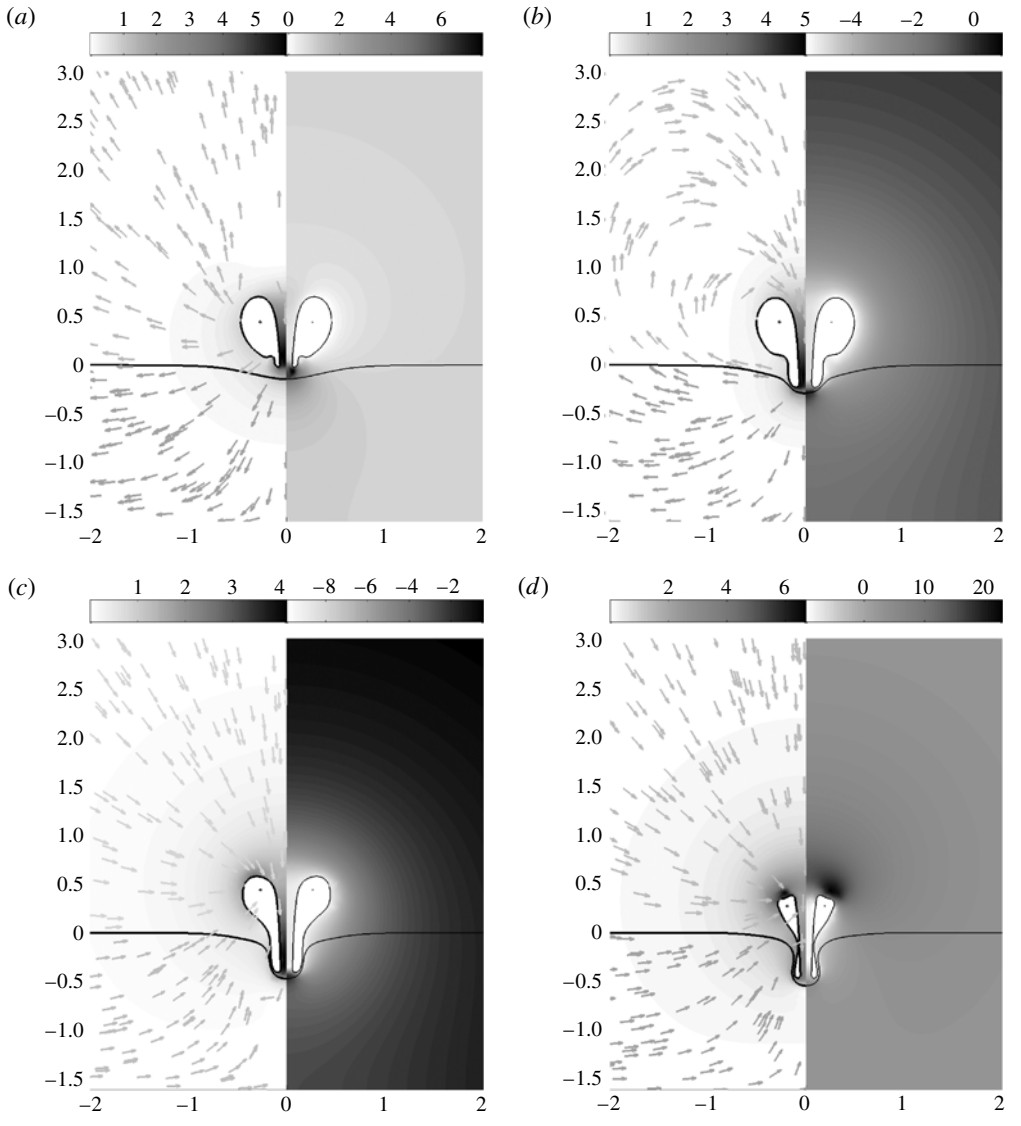

FIGURE 19. Post-impact flow fields for an acoustically driven cavitation bubble with identical parameters to figure 15, with a rigid wall located at $H = 1.6R_{max}$ from the initially flat interface: $t = 1.14$ (*a*); $t = 1.21$ (*b*); $t = 1.29$ (*c*); $t = 1.33$ (*d*).

The final frame is taken just after the overpressure has reached a maximum, and as can be clearly seen by the velocity field the bubble is recollapsing. Fluid near the interface is now flowing parallel to it in the direction of the bubble. A clearly visible feature is the formation of a hollow hemispherical pressure cap above the jet mouth, with a maximum pressure and velocity located at about $r = 0.4$. This will result in a secondary bubble jet forming from the outer edge of the ring. The bubble jet itself is still significantly faster than the fluid it is entering into, and a stagnation point will have formed between the jet and the liquid being forced upward by the decrease in bubble volume. This will inhibit the advancement of the forward bubble

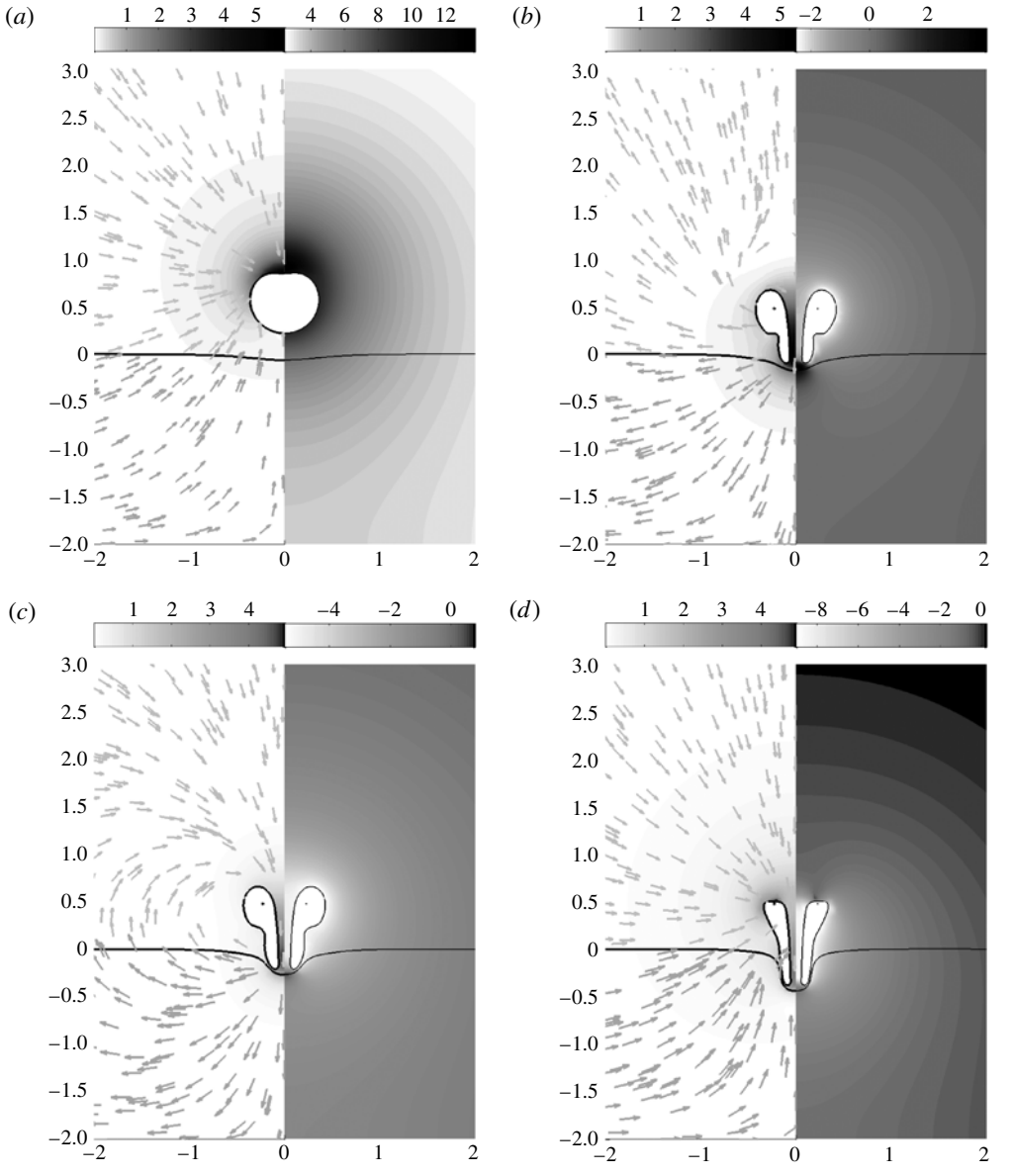

FIGURE 20. Toroidal behaviour of an acoustically driven bubble with identical parameters to figure 15, with the depth of the second fluid layer $H = 2.0$ maximum bubble radii: $t = 1.0$ (*a*); $t = 1.17$ (*b*); $t = 1.21$ (*c*); $t = 1.29$ (*d*).

lobe into the second fluid layer, which may be of significant benefit in drug-delivery applications.

5.3. *New experimental evidence of peeling*

Recently, the peeling phenomena observed for very shallow layer depths has been potentially been observed experimentally by Tomita *et al.* (2008). In these experiments, a backed layer of oil-based ink with a near uniform depth of 3 μm was submerged in a

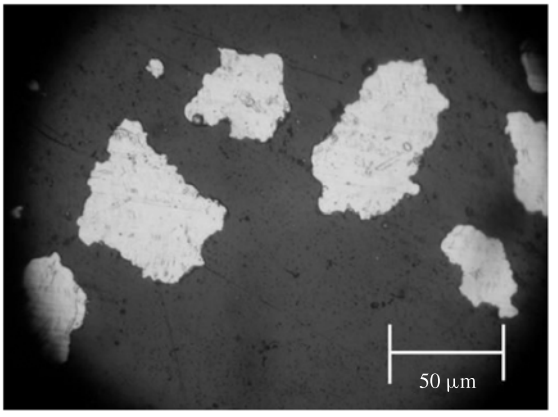

FIGURE 21. Experimental evidence of peeling of an oily ink layer by cavitation bubble interactions (Tomita *et al.* 2008).

water tank and insonated at 28 kHz. Photographic evidence showed that after treatment in this way, the grouping of cavitation filaments produced sufficiently large bubble clusters to remove the ink from the surface. The authors postulate this was due to both jet impact and a shear flow of water against the solid nickel surface. A photograph taken of the substrate and oil coating after the experiment is shown in figure 21.

The results presented here illustrate that a different physical mechanism may be appropriate. As such more detailed experiments should be performed to help identify the dominant phenomenon.

6. Summary

In this paper we have investigated various aspects of acoustically driven bubble behaviour relevant to biomedical applications. Membrane interactions have clearly demonstrated that bubble behaviour may not match that of simple rigid boundaries or free surfaces. Moreover, they have shown bubble actions to be significantly non-spherical, although jetting may not occur during the first few oscillations. More significantly however is the effect of including a backing plate to the second layer, a commonly used experimental method for examining bubble–cell interactions. This has shown that the semi-infinite fluid interactions of the type discussed in Leppinen *et al.* (2011) can be almost completely dominated by the interaction with the plate. By coincidence this has also illustrated a new mechanism for tissue damage, the peeling of the attached layer through the interaction with the re-expanding toroidal bubble. The occurrence of this phenomena is truly significant, and although the resultant damage has potentially been experimental realized, as for example the cornea specimen in figure 1, it would be extremely difficult to identify the mechanism without this numerical approach used in this paper. Previously, it was assumed that the removal of tissue about the impact site was due to the high shear rates accompanying the fluid jet Vogel *et al.* (1990). While this is no doubt important, the inertial interaction of the expanding forward bubble lobes provides an additional destructive mechanism. Moreover, this peeling provides an efficient method for removing unwanted material layers by literally lifting it off an attached surface, such as removing cholesterol from the aortic artery.

In terms of sonoporation and gene transfection, the investigation into the cell layer depth and standoff distance of a UCA has given great insight into the significant values of these parameters. In particular, the behaviour of a 2.5 μm UCA with similar characteristics to Sonovue, driven by a high-amplitude acoustic wave with megahertz frequency, has been investigated in detail. At shallow cell layer depths the peeling mechanism is observed, and the jetting motion will lead to a sonopore on the length scale of a cell. This of course will lead to the death of the target cell, although adjacent cells may in fact be porated through the stresses placed on them by the lifting mechanism. At cell layer depths greater than one maximum bubble radii, very different behaviour is observed. The distance from the rigid boundary allows the frontal lobe to elongate substantially, with the separating membrane being perturbed accordingly. Moreover, this is followed by the secondary collapse, which may separate the frontal lobe section away from the rear, physically injecting this section into the tissue layer. Clearly such an action would be hugely beneficial in transfection, as the damaged membrane appears to close up behind this potentially DNA enclosing segment. In addition, with the destruction of the UCA shell in this manner, the gaseous contents of the bubble are likely to dissolve into the surrounding fluid, and hence the bubble itself would rapidly disappear. One may therefore anticipate very limited subsequent collateral damage associated with the continued excitation of the UCA fragments, which naturally will promote the survival of the transfected cell.

REFERENCES

BLOMLEY, M. J. K., COOKE, J. C., UNGER, E. C., MONAGHAN, M. J. & COSGROVE, D. O. 2001 Microbubble contrast agents, a new era in ultrasound. *Br. Med. J.* **322**, 1222–1225.

BRUJAN, E. A., NAHEN, K., SCHMIDT, P. & VOGEL, A. 2001*a* Dynamics of laser-induced cavitation bubbles near an elastic boundary. *J. Fluid Mech.* **433**, 251–281.

BRUJAN, E. A., NAHEN, K., SCHMIDT, P. & VOGEL, A. 2001*b* Dynamics of laser-induced cavitation bubbles near elastic boundaries: influence of the elastic modulus. *J. Fluid Mech.* **433**, 283–314.

CALVISI, M. L., ILORETA, J. I. & SZERI, A. J. 2008 Dynamics of bubbles near a rigid surface subjected to a lithotripter shock wave. Part 2. Reflected shock intensifies non-spherical cavitation collapse. *J. Fluid Mech.* **616**, 63–97.

CHURCH, C. C. 1995 The effects of an elastic solid surface layer on the radial pulsations of gas bubbles. *J. Acoust. Soc. Am.* **97**, 1510–1521.

COSGROVE, D. O. 2006 Ultrasound contrast agents: an overview. *Eur. J. Radiol.* **60**, 324–330.

CURTISS, G. A., LEPPINEN, D. M., WANG, Q. X. & BLAKE, J. R. 2013 The interaction of bubbles with a density interface. Mathematical modelling and numerical implementation. *J. Comput. Phys.* (submitted).

FONG, S. W., KLASEBOER, E., TURANGAN, C. K., KHOO, B. C. & HUNG, K. C. 2006 Numerical analysis of a gas bubble near biomaterials in an ultrasound field. *Ultrasound Med. Biol.* **32** (6), 925–942.

KLASEBOER, E., HUNG, K. C., WANG, C., WANG, C. W., KHOO, B. C., BOYCE, P., DEBONO, S. & CHARLIER, H. 2005 Experimental and numerical investigation of the dynamics of an underwater explosion bubblenear a resilient/rigid structure. *J. Fluid Mech.* **537**, 387–413.

KLASEBOER, E. & KHOO, B. C. 2004*a* Boundary integral equations as applied to an oscillating bubble near a fluid–fluid interface. *Comput. Mech.* **33**, 129–138.

KLASEBOER, E. & KHOO, B. C. 2004*b* An oscillating bubble near an elastic material. *J. Appl. Phys.* **96** (10), 5808–5818.

KOIKE, H., TOMITA, N., AZUMA, H., TANIYAMA, Y., YAMASAKI, K., KUNUGIZA, Y., TACHIBANA, K., OGIHARA, T. & MORISHITA, R. 2005 An efficient gene transfer method mediated by ultrasound and microbubbles into the kidney. *J. Gene Med.* **7**, 106–116.

LEPPINEN, D. M., CURTISS, G. A., WANG, Q. X. & BLAKE, J. R. 2011 Bubble behaviour near a two fluid interface. In *WIMRC 3rd International Cavition Forum*, University of Warwick.

MARMOTTANT, P., VAN DER MEER, S., EMMER, M., VERSLUIS, M., DE JONG, N., HILGENFELDT, S. & LOHSE, D. 2005 A model for large amplitude oscillations of coated bubbles accounting for buckling and rupture. *J. Acoust. Soc. Am.* **118**, 3499–3505.

MIAO, H. & GRACEWSKI, S. M. 2008 Coupled FEM and BEM code for simulating acousticallyexcited bubbles near deformable structures. *Comput. Mech.* **42**, 95–106.

MILLER, D. L., BAO, S. & THRALL, B. D. 1997 Transfection of a reporter plasmid into cultured cells in vitro. *Ultrasound Med. Biol.* **23** (6), 953–959.

MILLER, D. L., PISLARU, S. V. & GREENLEAF, J. F. 2002 Sonoporation: mechanical DNA delivery by ultrasonic cavitation. *Somatic Cell Mol. Genetics* **27** (1), 115–134.

MILLER, D. & QUDDUS, J. 2000 Diagnostic ultrasound activation of contrast agent gas bodies induces capillary rupture in mice. *Proc. Natl Acad. Sci. USA* **97**, 10179–10184.

PRENTICE, P., CUSCHIERI, A., DHOLAKIA, K., PRAUSNITZ, M. & CAMPBELL, P. 2005 Membrane disruption by optically controlled microbubble cavitation. *Nat. Phys.* **1**, 107–110.

RAPOPORT, N., PITT, W. G., SUN, H. & NELSON, J. L. 2003 Drug delivery in polymeric micelles: from in vitro to in vivo. *J. Control. Release* **91**, 85–95.

SEEMANN, S., HAUFF, P., SHULTZ-MOSGAU, M., LEHMANN, C. & RESKA, R. 2002 Pharmaceutical evaluation of gas-filled microparticles as gene delivery system. *Pharmaceut. Res.* **19** (3), 250–257.

SKOLARIKOS, A., ALIVIZATOS, G. & ROSETTE, J. 2006 Extracorporeal shock wave lithotripsy 25 years later: complications and their prevention. *Eur. Urol.* **50**, 981–990.

TOMITA, Y., INABA, T., UCHIKOSHI, R. & KODAMA, T. 2008 Peeling off effect and damage pit formation by ultrasonic cavitation. *Sci. Bull. Politehnica Univ. Timisoara Trans. Mech.* **53**, 19–24.

TURANGAN, C. K., ONG, G. P., KLASEBOER, E. & KHOO, B. C. 2006 Experimental and numerical study of transient bubble-elastic membrane interaction. *J. Appl. Phys.* **100**, 054910.

VOGEL, A., SCHWEIGNER, P., FRIESER, A., ASIYO, M. N. & BIRNGRUBER, R. 1990 Intraocular Nd:YAG laser surgery: light tissue interaction, damage range, and reduction of collateral effects. *J. Quant. Electron.* **26**, 2240–2260.